Radiometric Cross Calibration of HY-1C/COCTS Based on Sentinel-3/OLCI

Yong Xie, *Senior Member, IEEE*, Duo Feng, Wen Shao, Jie Han, and Yidan Chen

***Abstract*—The on-orbit radiometric calibration of spaceborne sensors is the foundation of quantitative remote sensing, and the calibration accuracy directly affects the quality of quantitative remote sensing products. The wide swath of the Chinese Ocean Color and Temperature Scanner (COCTS) onboard the HY-1C satellite makes it difficult to ignore errors caused by viewing angles during calibration. Thus, this article proposes a cross-calibration method based on the bottom-of-atmosphere (BOA) and top-of-atmosphere (TOA) spectral band adjustment factors (SBAFs). This method cross calibrates the COCTS sensor after correcting viewing geometry and radiometric differences. It is based on the Sentinel-3/ocean and land color instrument (OLCI) sensor. First, time-series data from the OLCI sensor were used to select calibration points in the Dunhuang area. Subsequently, the bidirectional reflectance distribution function (BRDF) for each corresponding spectral band of the OLCI sensor was constructed point by point. Next, the BOA and TOA SBAFs were calculated using the interpolated continuous spectra obtained from MOD09GA products. After correcting for the BRDF and SBAF, cross calibration between COCTS and OLCI was achieved. The results showed that the BOA SBAF model achieved higher precision calibration coefficients than the TOA SBAF model, with errors in each band below 5.76%. The proposed method can provide technical support for the cross calibration of wide-swath sensors.**

***Index Terms*—Bidirectional reflectance distribution function (BRDF), Chinese Ocean Color and Temperature Scanner (COCTS), cross calibration, ocean and land color instrument (OLCI), spectral band adjustment factor (SBAF).**

I. INTRODUCTION

THE HaiYang-1C satellite was launched on September 7, 2018. It is equipped with the Chinese Ocean Color and Temperature Scanner (COCTS), which provides global distribution data on chlorophyll, particles, organic carbon, primary productivity, and other biogeochemical parameters related to the ocean [1]. Ocean color data are important for understanding global carbon cycling and ocean–atmosphere interactions [2]. The radiometric characteristics of satellite sensors are subject to degradation because of factors, such as changes in the on-orbit spatial environment [3]. Thus, through prompt on-orbit radiometric calibration, the accuracy of quantitative remote sensing products for ocean-related parameters can be ensured.

The calibration methods commonly employed in China include on-site calibration, on-orbit calibration, and cross calibration [4]. Cross calibration offers high precision, low resource requirements, and the ability to efficiently construct time series; thus, it has recently been widely applied. Liu et al. [5] conducted a long-term cross calibration of Huanjing-1A/CCD1 and discussed the sensor degradation over its 12 years of on-orbit operation. Han et al. [6] considered the different integration times of the Gaofen-4 (GF-4)/panchromatic and multispectral sensor and developed a cross-calibration method based on radiometric grid adjustment to achieve consistency with high official calibration coefficients. Farhad et al. [7] conducted cross calibration between the Landsat 8/operational land imager (OLI) and the Sentinel-2A/multispectral instrument (MSI) after correcting radiometric differences using the bidirectional reflectance distribution function (BRDF). They discovered the most significant differences in the blue and red spectral bands. Han and Xie [8] used the absolute radiometric calibration coefficient of the first camera to establish the correlation model of the digital number and apparent radiance among adjacent camera images. They realized color uniformity processing among images. Juan et al. [9] compared two cross-calibration methods based on images and radiative transfer models using the Dunhuang radiometric calibration site (DRCS) as a platform. The study showed that when the satellite viewing zenith angle was below 20°, the image-based method achieved the highest accuracy; when it exceeded 20°, the radiative-transfer-model-based method performed better. Fang et al. [10] used the hyperspectral data provided by the United States Geological Survey to correct the radiation difference between the GF-1/wide field of view and the Landsat8/OLI and cross calibrated it, achieving an average error and uncertainty below 5% and 8%, respectively. Zhou et al. [11] comprehensively discussed the influence of the BRDF in desert and forest areas on cross-calibration results.

Although the aforementioned studies achieved numerous results in this field, their research mostly involved medium- to high-resolution sensors with narrow viewing widths. For wide-swath sensors, such as the COCTS, differences in viewing geometry can significantly affect calibration accuracy, thereby

Manuscript received 25 March 2024; revised 13 May 2024; accepted 16 May 2024. Date of publication 20 May 2024; date of current version 31 May 2024. This work was supported in part by National Natural Science Foundation of China under Grant 42176176, in part by National Natural Science Foundation Cultivation Project of Xuchang University under Grant 2022GJPY007 and Grant 2023GJPY019, in part by Science and Technology of Henan Province under Grant 242102320005, in part by Key Scientific Research Project Plan of University in Henan Province under Grant 24A420004, and in part by the Land Observation Satellite Supporting Platform of National Civil Space Infrastructure Project. *(Corresponding author: Jie Han.)*

Yong Xie, Duo Feng, Wen Shao, and Yidan Chen are with the School of Geographical Sciences, Nanjing University of Information Science and Technology, Nanjing 210044, China (e-mail: xieyong@nuist.edu.cn; fffduo@163.com; wenshao@nuist.edu.cn; 20221210009@nusit.edu.cn).

Jie Han is with the School of Geography and Geomatics, Xuchang University, Xuchang 461000, China (e-mail: hanjie@radi.ac.cn).

Digital Object Identifier 10.1109/JSTARS.2024.3403107

TABLE I
OLCI AND COCTS INFORMATION

Sensor	Spectral Band Number	Central wavelengths (nm)	Quantization (bits)	Sensor	Spectral Band Number	Central wavelengths (nm)	Quantization (bits)
OLCI	Oa2	412.5	16	COCTS	B1	412	16
	Oa3	442.5			B2	443	
	Oa4	490			B3	490	
	Oa5	510			B4	520	
	Oa6	560			B5	565	

affecting quantitative applications. Thus, this study obtained high-precision calibration coefficients and reduced errors caused by differences in viewing geometry and sensor radiometry. To achieve this, we employed a time series of Sentinel-3/ocean and land color instrument (OLCI) images to construct a BRDF model for calibration points in the DRCS. In addition, based on MOD09GA surface reflectance products and spectral interpolation, continuous spectral data were obtained for the calibration points [12]. Subsequently, cross calibration was performed using the bottom-of-atmosphere (BOA) and top-of-atmosphere (TOA) spectral band adjustment factors (SBAFs). Finally, we verified the accuracy of the calibration results. The study findings contribute to the determination of the optimal cross-calibration scheme for the COCTS sensor, providing technical support for monitoring the radiometric performance of the COCTS sensor during its on-orbit operation.

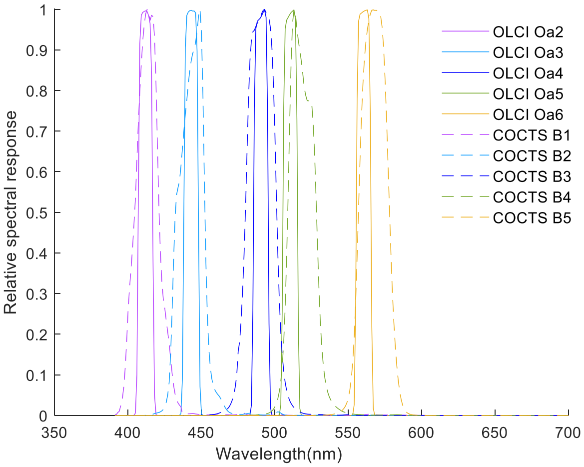

Fig. 1. Spectral response functions of Sentinel-3/OLCI and HY-1C/COCTS.

II. SATELLITES, TEST SITE, AND DATASETS

A. Satellites

HY-1C is a sun-synchronous orbit satellite with an orbit span of 782 km, an inclination angle of 98.522°, and a local equator crossing time of 10:30 A.M. ± 30 min. The COCTS sensor aboard the satellite is a moderate resolution imaging tool with a swath width of 2900 km, spatial resolution of 1100 m, quantization level of 16 bits, and viewing coverage cycle of one day. It monitors global ocean color and sea surface temperature for applications and research in marine biology, ocean ecology conservation, marine disaster prevention, and climate change. In addition, it is used to observe sea ice, shallow marine topography, ocean current characteristics, atmospheric aerosols over the sea surface, and research and surveys of terrestrial natural resources.

With its high-precision onboard calibrator, the Sentinel-3/OLCI, known for its excellent calibration accuracy (radiometric uncertainty better than 2% [13]), is the reference sensor for calibrating the COCTS. The new-generation optical sensor, OLCI, is based on the design of Envisat's medium-resolution imaging spectrometer (MERIS). However, it offers higher spectral resolution and more spectral channels than the MERIS. It has a swath width of 1270 km, a spatial resolution of 300 m, a quantization level of 16 bits, and a revisit period of less than 1.5 days [14]. This study used full-resolution (300-m) OLCI images (L1B) obtained from the European Space Agency data center as references. The central wavelengths and quantization levels for the OLCI and the COCTS are listed in Table I. The spectral response functions for the corresponding five bands of the OLCI and COCTS sensors are shown in Fig. 1.

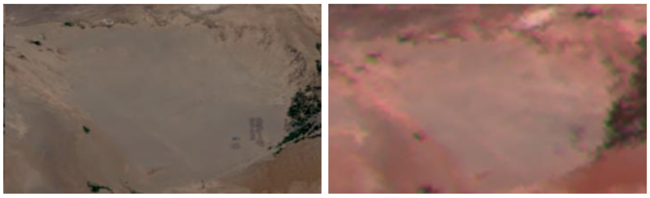

Fig. 2. OLCI (left) and COCTS (right) images of the DRCS.

B. Test Site

The DRCS, a nationally designated radiometric calibration site in China, has gained international recognition because of its flat terrain, uniform surface, and good radiometric stability (see Fig. 2) [15]. It is located at an altitude of approximately 1200 m, with a temporal stability that is better than 5% [16]. It is commonly used for cross calibration and on-site calibration [17]. It functions as a radiative transfer platform for assessing radiometric differences between two sensors and monitoring the on-orbit radiometric performance degradation of sensors [18]. The DRCS has provided on-site services for absolute radiometric calibration for several Chinese satellites, including

TABLE II
NUMBER OF SELECTED IMAGES FROM 2019 TO 2021

Years	Numbers of OLCI images used for BRDF calculation	Numbers of calibration image pairs of COCTS and OLCI
2019	26	6
2020	35	9
2021	44	19

TABLE III
RELATIVE ERRORS IN BOA AND TOA SBAF CALCULATIONS BETWEEN MEASURED AND INTERPOLATED SPECTRA

	BOA SBAF					TOA SBAF				
	B1	B2	B3	B4	B5	B1	B2	B3	B4	B5
Calculation of SBAF using measured spectrum	1.0135	1.0038	1.0000	1.0288	1.0132	0.9929	1.0016	1.0000	0.9939	0.9851
Calculation of SBAF using interpolated spectrum	1.0103	0.9992	1.0008	1.0252	1.0199	0.9913	0.9996	1.0004	0.9860	0.9880
Relative error (%)	0.31	0.47	0.08	0.35	0.07	0.17	0.20	0.04	0.80	0.29

the China–Brazil Earth Resource Satellite [19], Huan Jing [20], and Gaofen Satellite series [21].

C. Datasets

The OLCI and the COCTS are wide-swath sensors; thus, it is necessary to consider the differences in the viewing geometry of both the sensors. The study used 105 cloud-free OLCI images captured over the DRCS from 2019 to 2021 to construct a BRDF model. All the parameters required for constructing the BRDF model were extracted from the OLCI images. Concomitantly, COCTS images of the DRCS captured within 1 h after the OLCI images were obtained were selected as calibration images [22]. The distribution of selected images for the BRDF calculation and calibration images is shown in Table II . The geometric information of the calibration images is shown in Fig. 3. In addition, MOD09GA and MOD04 products were used to obtain BOA reflectance and aerosol optical depth (AOD) at 550 nm, respectively, at the calibration points.

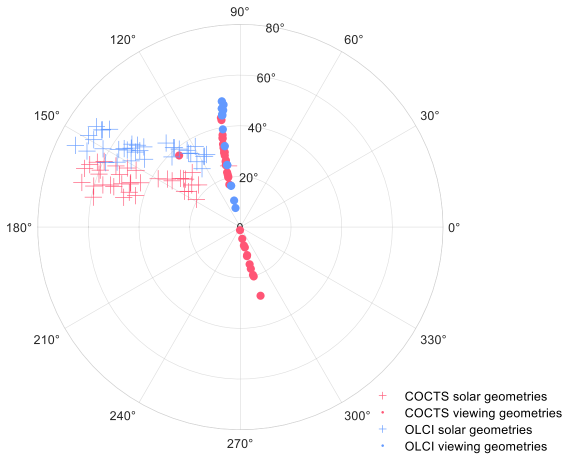

Fig. 3. Geometric information of calibration scenes.

III. METHODOLOGY

This study constructed two cross-calibration methods for building BOA and TOA SBAF models and compared them with the ray-matching model. The construction of the calibration model was as follows.

First, a time series of cloud-free OLCI images over the DRCS for three years was selected. Uniform areas were selected as calibration points for subsequent use. Next, a Ross–Li BRDF model was constructed using a kernel-driven approach with the OLCI time-series images. Thereafter, the BRDF model was used to compute the spectral reflectance under geometric conditions for the OLCI and COCTS sensors, obtaining BRDF correction coefficients. Afterward, SBAF correction was applied to correct errors between the sensors caused by spectral response function mismatch. Finally, based on the BRDF and SBAF correction coefficients, the theoretical reflectance of the COCTS in different models was simulated and converted into radiance. The COCTS calibration coefficients were calculated to construct a time series.

A. Selection of Calibration Points

The coefficient of variation method was employed to select calibration points [23]. The coefficient of variation was limited to 2% within each 11 × 11 pixel area (3300 m × 3300 m) of the time series of cloud-free OLCI images spanning three years, totaling

105 scenes. Any area with a coefficient of variation below 2% was selected as a calibration point. After screening, 4638 calibration points were selected. During the cross-calibration process, the COCTS images utilized the average digital number (DN) values within a 3×3 pixel area corresponding to the latitude and longitude coordinates.

B. Construction of the BRDF Model

The BRDF model is a function of the viewing zenith, solar zenith, and relative azimuth angles of the sensor, which can be used to establish a quantitative relationship between spectral reflectance and viewing geometry [11]. Sentinel-3 does not provide BRDF coefficients; thus, this study adopted the Ross–Li BRDF model. Using the OLCI time-series data, viewing geometry parameters and the apparent reflectance of the calibration points were extracted. The corresponding parameters were input into the following equation to obtain the coefficients of the BRDF model:

$$\rho(\theta,\vartheta,\varphi) = f_{\mathrm{iso}} + f_{\mathrm{vol}}K_{\mathrm{vol}}(\theta,\vartheta,\varphi) + f_{\mathrm{geo}}K_{\mathrm{geo}}(\theta,\vartheta,\varphi) \quad (1)$$

where $\rho(\theta,\vartheta,\varphi)$ is the bidirectional spectral reflectance, and f_{iso}, f_{vol}, and f_{geo} refer to the weight coefficients of the respective kernel functions to be retrieved. $K_{\mathrm{vol}}(\theta,\vartheta,\varphi)$ represents the volumetric scattering kernel, and $K_{\mathrm{geo}}(\theta,\vartheta,\varphi)$ represents the geometric-optical kernel. They are calculated with the viewing zenith angle, θ, solar zenith angle, ϑ, and the relative azimuth angle, φ.

C. Calculation of the BRDF Correction Coefficient

Based on the geometric parameters of the OLCI and the COCTS and the calculated BRDF correction coefficients, the surface reflectances, $\rho_{O_i\_\mathrm{brdf}}$ and $\rho_{C_i\_\mathrm{brdf}}$, of band i of the OLCI and the COCTS were simulated under OLCI geometric conditions. The BRDF correction coefficients, C_i, were calculated using the following equation:

$$C_i = \frac{\rho_{C_i\_\mathrm{brdf}}}{\rho_{O_i\_\mathrm{brdf}}}. \quad (2)$$

D. Spectral Matching

Fig. 1 shows the difference in the spectral response functions of both the sensors. However, it is challenging to determine the time-series measured reflectance and use it to calculate the SBAF coefficients for the five bands. Han et al. [24] addressed the issue of the lack of corresponding reference bands for the cross calibration of GF-6 in the DRCS using the spectral interpolation method. This study employed the cubic polynomial interpolation method to interpolate the MOD09GA product. The calculation of the convolution for the equivalent reflectance of the corresponding bands involved the continuous spectrum. The convolution calculation formula was as follows:

$$\rho_{\mathrm{satellite}}^{\mathrm{BOA}} = \frac{\int_b^a \rho^{\mathrm{BOA}}(\lambda)\tau(\lambda)}{\int_b^a \tau(\lambda)d\lambda} \quad (3)$$

where $\rho_{\mathrm{satellite}}^{\mathrm{BOA}}$ is the equivalent reflectance of satellite bands obtained after convolution. a and b are the upper and lower limits of the corresponding band wavelengths, respectively. λ is the wavelength, and ρ^{BOA} is the actual measured reflectance at the corresponding wavelength. Finally, $\tau(\lambda)$ is the spectral response value.

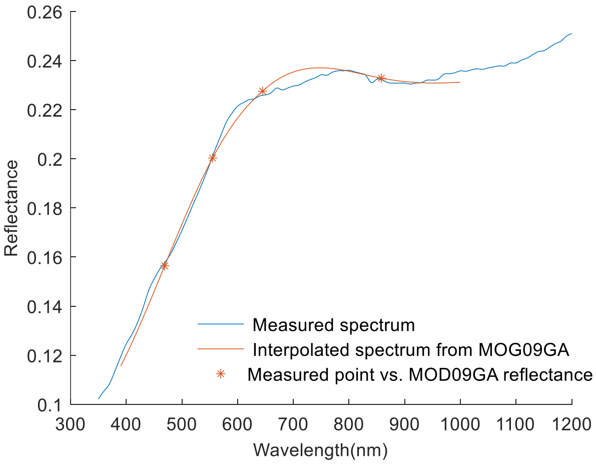

Fig. 4. Measured surface reflectance and MOD09GA interpolation results for August 5, 2014.

Using the satellite-convolved equivalent ground reflectance, $\rho_{\mathrm{COCTS}_i}^{\mathrm{BOA}}$ and $\rho_{\mathrm{OLCI}_i}^{\mathrm{BOA}}$, the BOA SBAF coefficient, $\mathrm{SBAF}_i^{\mathrm{BOA}}$, for band i was calculated by computing the ratio of $\rho_{\mathrm{COCTS}_i}^{\mathrm{BOA}}$ to $\rho_{\mathrm{OLCI}_i}^{\mathrm{BOA}}$

$$\mathrm{SBAF}_i^{\mathrm{BOA}} = \frac{\rho_{\mathrm{COCTS}_i}^{\mathrm{BOA}}}{\rho_{\mathrm{OLCI}_i}^{\mathrm{BOA}}}. \quad (4)$$

For the TOA SBAF, the simulated TOA reflectances of the COCTS and the OLCI under the geometric condition of the COCTS were derived using the 6S, viewing geometry of the COCTS, and continuous spectrum over the DRCS. It should be noted that the atmospheric conditions are set as follows: April to September is considered mid-latitude summer, while October to March is mid-latitude winter [5]. In addition, the AOD at 550 nm on the calibration days is extracted from the MOD04 aerosol product. The aerosol type is designated as desert, and the elevation is set to 1200 m. Subsequently, the TOA SBAF correction coefficient, $\mathrm{SBAF}_i^{\mathrm{TOA}}$, is calculated using the following formula:

$$\mathrm{SBAF}_i^{\mathrm{TOA}} = \frac{\rho_{\mathrm{COCTS}_i}^{\mathrm{TOA}}}{\rho_{\mathrm{OLCI}_i}^{\mathrm{TOA}}}. \quad (5)$$

For the measured land spectrum at the calibration point in the central area of the DRCS on August 5, 2014, the continuous spectral curve of the measured point was obtained via MOD09GA interpolation. Thereafter, BOA and TOA SBAFs were calculated separately. Fig. 4 shows the measured and interpolated surface reflectance. The spectral shapes of both surface reflectances are similar. Table III presents the relative errors between the measured and interpolated spectra for the BOA and TOA SBAF coefficients. The maximum relative errors for both the coefficients were low at 0.47% and 0.80%, respectively.

TABLE IV
MREs OF THE BRDF MODEL

	Oa2	Oa3	Oa4	Oa5	Oa6
2019	2.07%	2.27%	2.79%	3.06%	3.90%
2020	3.93%	3.91%	3.87%	3.83%	3.94%
2021	3.75%	3.62%	3.62%	3.73%	4.35%

E. Construction of Cross-Calibration Models

Based on the established BRDF model and the BOA and TOA SBAF coefficients, we established cross-calibration models for the BOA and TOA SBAFs. The process was as follows.

1) The TOA reflectance, $\rho_{\mathrm{OLCI}_i}^{\mathrm{TOA}}$, of OLCI band i was corrected using the calculated BRDF correction coefficients and BOA and TOA SBAF coefficients. The correction formula was as follows:

$$\rho_{\mathrm{COCTS}_i}^{\mathrm{BOASBAF}} = C_i \times \mathrm{SBAF}_i^{\mathrm{BOA}} \times \rho_{\mathrm{OLCI}_i}^{\mathrm{TOA}} \tag{6}$$

$$\rho_{\mathrm{COCTS}_i}^{\mathrm{TOASBAF}} = C_i \times \mathrm{SBAF}_i^{\mathrm{TOA}} \times \rho_{\mathrm{OLCI}_i}^{\mathrm{TOA}}. \tag{7}$$

2) The simulated TOA radiance of the COCTS images, L_{COCTS_i}, was calculated as follows:

$$L_{\mathrm{COCTS}_i} = \frac{\rho_{\mathrm{COCTS}_i}^{\mathrm{TOA}} \times E_{\mathrm{SUN}}^{\mathrm{COCTS}_i} \times \cos\vartheta}{\pi d^2} \tag{8}$$

where L_{COCTS_i} is the TOA radiance of the COCTS for band i, $\rho_{\mathrm{COCTS}_i}^{\mathrm{TOA}}$ is the theoretical TOA reflectance of the COCTS, $E_{\mathrm{SUN}}^{\mathrm{COCTS}_i}$ is the solar irradiance of the COCTS, ϑ is the solar zenith angle of the COCTS, and d is the distance between the Sun and the earth.

3) The cross-calibration formulas for the three models were as follows:

$$\frac{\rho_{\mathrm{COCTS}_i}^{\mathrm{SBAF}} \times E_{\mathrm{SUN}}^{\mathrm{COCTS}_i} \times \cos\vartheta}{\pi d^2} = \mathrm{Gain}_{\mathrm{COCTS_i}}^{\mathrm{SBAF}} \times \mathrm{DNCOCTS_i} + \mathrm{Offset}_{\mathrm{COCTS_i}}^{\mathrm{SBAF}} \tag{9}$$

$$L_{\mathrm{COCTS}_i} = \mathrm{Gain}_{\mathrm{COCTS_i}} \times \mathrm{DNCOCTS_i} + \mathrm{Offset}_{\mathrm{COCTS_i}}. \tag{10}$$

The calibration formula for the different SBAF models is shown in (9), where $\mathrm{Gain}_{\mathrm{COCTS}_i}^{\mathrm{SBAF}}$ and $\mathrm{Offset}_{\mathrm{COCTS}_i}^{\mathrm{SBAF}}$ are the gain and offset in the calibration coefficients of the different SBAF models, respectively. The calibration formula for the ray-matching model is shown in (10), where $\mathrm{Gain}_{\mathrm{COCTS}_i}$ and $\mathrm{Offset}_{\mathrm{COCTS}_i}$ are the gain and offset in the calibration coefficients of the ray-matching model, respectively.

IV. RESULTS

A. Validation of BRDF Model Accuracy

The BRDF coefficients were calculated corresponding to the calibration points for the five bands using the OLCI time-series images (see Table IV). The accuracy of the BRDF model was validated by calculating the average relative error between the apparent reflectance from the OLCI sensor (true values) and the reflectance from the BRDF model (predicted values). The calculation formula was as follows:

$$\mathrm{MRE}_i = \frac{\sum_1^N \frac{|\mathrm{BRDF}_{i_n} - \mathrm{REF}_{i_n}|}{\mathrm{REF}_{i_n}} \times 100\%}{N} \tag{11}$$

where MRE_i is the mean relative error for band i, and BRDF_{i_n} is the predicted value of the BRDF model for the nth calibration point in band i. REF_{i_n} is the TOA reflectance obtained from OLCI viewing for the nth calibration point in band i ($n = 1, 2, 3, \ldots, N$).

The minimum average relative error for the five bands over the three years occurred in 2019, with a minimum value of 2.07%. The maximum average relative error occurred in 2021 for Oa6, with a maximum value of 4.35%. The average relative errors for all the bands in all the years were below 4%, except for Oa6 in 2021. Compared with the average relative errors of the BRDF model constructed by Han et al. [24] for the moderate-resolution imaging spectroradiometer (MODIS) sensor, the average relative errors of the present BRDF model were relatively small. Thus, the model can be employed to correct geometric viewing differences during cross calibration.

B. Results of SBAF Coefficients

The MOD09GA-calibrated point surface reflectance was interpolated using the cubic polynomial. The BOA and TOA SBAFs for the calibration scene dates were calculated, and a time series was constructed. Fig. 5 shows the time series.

In the BOA SBAF time series, the BOA SBAF range was 1.000–1.044 (all exceeding 1). In addition, the BOA SBAF values in B4 were consistently the highest, whereas B3 exhibited the lowest values. The TOA SBAF range was 0.9753–1.0093. Upon simulation from BOA to TOA, the SBAFs in B1 and B5 decreased below 1. Notably, the TOA SBAF in B4 fluctuated around 1, and the TOA SBAF values were relatively close across most dates.

C. Calibration Results

The calibration coefficients for the calibration image pairs were computed using the ray-matching model and the BOA and TOA SBAF models. Figs. 6– 8 illustrate the time series of the gains and offsets for the three calibration models. The gains for the five bands in the three calibration models were within the range of 0.0032–0.0052, with most values between 0.0038 and 0.0050. In addition, the gains based on the ray-matching model ranged from −20 to 40, which were larger than those of the BOA and TOA SBAF models. Moreover, the gain values for B1 were consistently the lowest among the five bands, whereas the offsets were mostly at their maximum. The calibration coefficients from the BOA and TOA SBAF models were closer to each other.

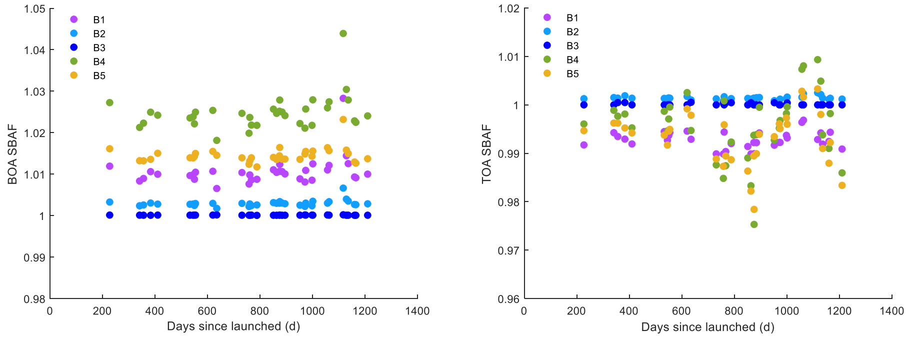

Fig. 5. Time series of the BOA SBAF (left) and the TOA SBAF (right).

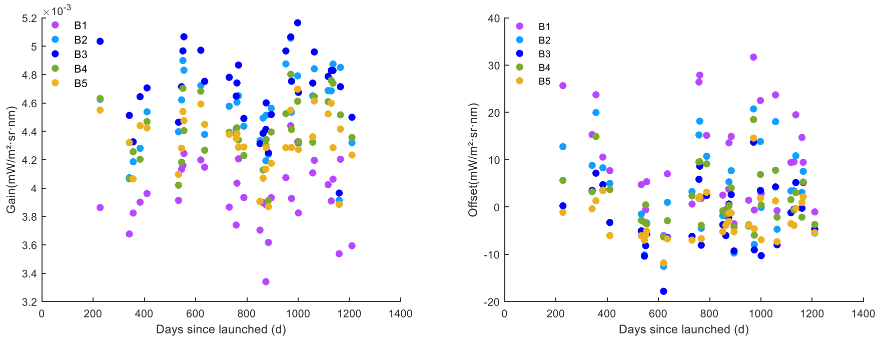

(a) (b)

Fig. 6. Time series of calibration coefficients based on the ray-matching model. (a) Gains. (b) Offsets.

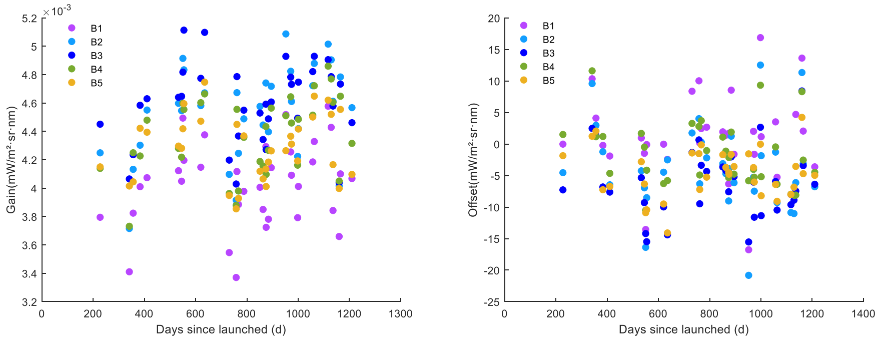

(a) (b)

Fig. 7. Time series of calibration coefficients based on the BOA SBAF model. (a) Gains. (b) Offsets.

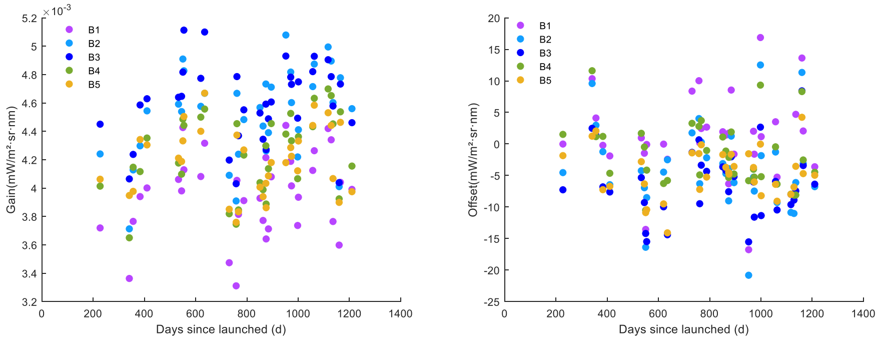

(a) (b)

Fig. 8. Time series of calibration coefficients based on the TOA SBAF model. (a) Gains. (b) Offsets.

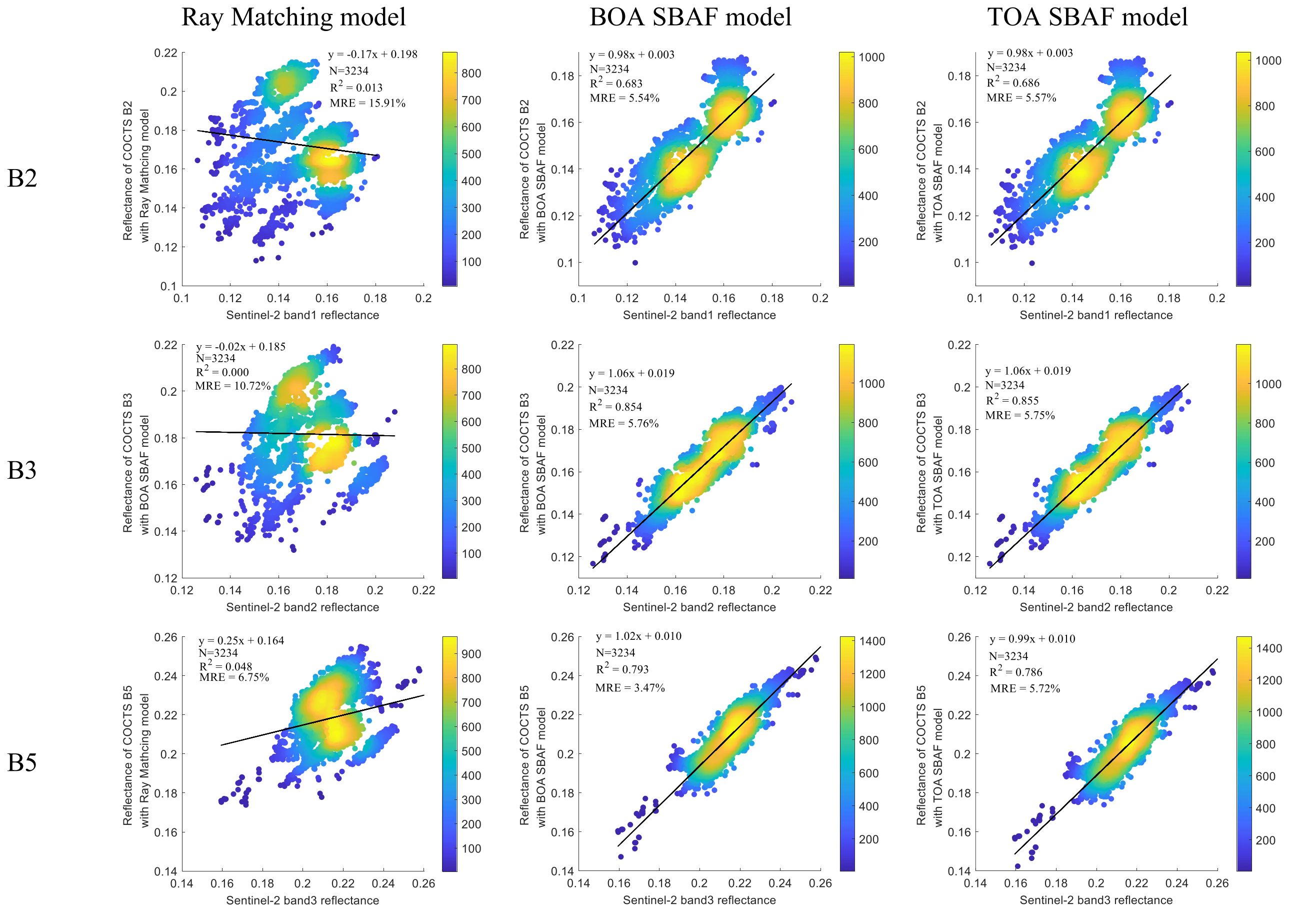

Fig. 9. Validation points and fitting plots for each band and model.

D. Validation Cross-Calibration Results

The calibration accuracy of the COCTS sensor was verified using the surface reflectance products (L2A) of the Sentinel-2/MSI sensor around the DRCS. Three bands of the COCTS (blue, cyan, and green) and the MSI were selected for their consistency and similar central wavelengths. Due to the significant difference in spatial resolution between the MSI sensor with spatial resolutions of 60, 10, and 10 m for its corresponding bands and the COCTS sensor with a spatial resolution of 1100 m, a specific approach was adopted for selecting validation points. For MSI band 1 (with a resolution of 60 m), a 55 × 55 pixel area (3300 m × 3300 m) was selected. For Bands 2 and 3 (with resolutions of 10 m), a larger area of 331 × 331 pixels (3310 m × 3310 m) was chosen. In addition, corresponding points on the HY-1C/COCTS sensor were selected in a 3 × 3 pixel area (3300 m × 3300 m). The coefficient of variation within these areas was calculated, and if it was less than 2%, the average value within the area was used as the validation point. Ten validation image pairs were selected from different times and areas. Following the same method as that described for calibration point extraction, 3234 validation points were extracted.

TABLE V
AVERAGE RELATIVE ERRORS FOR THE THREE MODELS

Model	B2	B3	B5
Ray-matching model	15.91%	10.72%	6.75%
BOA SBAF model	5.54%	5.76%	3.47%
TOA SBAF model	5.57%	5.75%	5.72%

During validation, the COCTS images were atmospherically corrected using the 6S radiative transfer model, converting the calibrated radiance into surface reflectance. During the validation process, MSI surface reflectance products were used as ground truth values for fitting, and the average relative error of the COCTS images after atmospheric correction was calculated.

Fig. 9 and Table V show that the ray-matching model performed poorly in the R^2 and MRE aspects. The BOA and TOA SBAF models exhibited similar R^2 values, with a maximum difference of 0.007. The BOA SBAF model achieved the lowest MRE at 3.47%, whereas the TOA SBAF model achieved the lowest MRE at 5.57%. The BOA SBAF model demonstrated higher precision than the TOA SBAF model, with the lowest MRE being 5.54% and 3.47% for Bands 2 and 5, respectively. Conversely, for Band 3, the TOA SBAF model outperformed others with an MRE of 5.75%. The MRE of the BOA SBAF model was only 0.01% lower than that of the TOA SBAF model.

TABLE VI
RELATIVE ERRORS FOR THE TWO MODELS USING THE CUBICSPLINE INTERPOLATION METHOD

Model	B2	B3	B5
BOA SBAF	5.69%	5.82%	3.61%
TOA SBAF	5.74%	5.80%	5.63%

TABLE VII
RELATIVE ERRORS FOR THE TWO MODELS USING BRDF IMAGES

Model	B2	B3	B5
BOA SBAF	6.08%	5.86%	3.50%
TOA SBAF	6.22%	5.83%	5.74%

TABLE VIII
RELATIVE ERRORS FOR THE TWO MODELS AFTER MOVING ONE PIXEL

Model	B2	B3	B5
BOA SBAF	5.92%	5.88%	3.57%
TOA SBAF	6.10%	5.87%	5.83%

Thus, the cross-calibration method using the BOA SBAF model was more suitable for the COCTS sensor.

V. DISCUSSIONS

A. Influence of Interpolation Methods on Cross-Calibration Results

For the proposed cross-calibration method, the suitability of using cubic polynomial interpolation to obtain the continuous spectral interpolation of the DRCS is subject to further discussion. Thus, we replaced cubic polynomial interpolation with cubic spline interpolation for the continuous spectral interpolation in the DRCS.

Table VI, compared with Table V, presents the average relative errors obtained using the cubic spline interpolation method, which were very close to those obtained using the cubic polynomial interpolation method. The maximum difference in the average relative errors was 0.17%. Thus, for the proposed cross-calibration method, the cubic polynomial interpolation and cubic spline interpolation methods were suitable for interpolating continuous spectra in the DRCS.

B. Influence of BRDF Correction on Cross-Calibration Results

During the cross-calibration method, BRDF correction was computed based on the BRDF coefficients corresponding to each year, derived from three years of BRDF modeling. We are yet to determine if this method is suitable for BRDF correction in the DRCS. Thus, we constructed a set of BRDF coefficients using BRDF images from three years.

Compared with Table V, Table VII presents the average relative errors using a single set of BRDF coefficients for calibration. The average relative errors obtained using a single set of BRDF coefficients slightly increased by 0.65%. This indicated that the method employed for BRDF model construction had a relatively minor impact on the proposed cross-calibration method.

C. Influence of Geometric Matching Errors on Cross-Calibration Results

In the process of cross calibration, obtaining accurate calibration information is crucial. However, geometric matching errors among image pairs can affect calibration accuracy. Therefore, the DN values of the new COCTS image are extracted by moving both rows and columns of the image by one pixel (1100 m). Subsequently, the new cross-calibration results are recalculated using the OLCI original image and the shifted COCTS image with the BOA and TOA SBAF models. The accuracy of the cross-calibration results is verified using the same MSI image.

Compared with Table V, Table VIII presents the average relative errors after shifting the COCTS images. The average relative errors obtained after shifting by one pixel are very close to the average relative errors before the shift. The maximum increase in relative average error is only 0.53%. This indicates that the geometric matching errors of the calibration image pairs in the study have minimal impact on the calibration accuracy.

VI. CONCLUSION

In this study, two radiometric cross-calibration methods applied with the TOA and BOA SBAF models are developed and compared to address the wide-swath characteristics of the COCTS sensor using the DRCS as the study area and the OLCI sensor as the radiometric reference. Using OLCI images and MODIS products as reference information, spectral reflectance of DRCS is extracted from the valid time-series OLCI images. Then, a high-precision BRDF model is constructed, and BRDF kernel model calibration coefficients are calculated. Subsequently, the cubic polynomial was employed to obtain continuous spectra for the calibration points, and the BOA and TOA SBAFs were calculated to correct sensor radiometric differences. Finally, by considering BRDF and SBAF corrections, high-precision in-orbit radiometric calibration was achieved for the COCTS sensor.

The validation results showed that considering BRDF and SBAF corrections, the precision of the cross-calibration coefficients varied by up to 10.38%, significantly higher than that without any correction. The calibration coefficients derived using the BOA SBAF model exhibited high accuracy. The average relative error of the calibration coefficients obtained using the BOA SBAF model is 3.47%, while that of the TOA SBAF model is 5.57%. The maximum difference in error between the two models is only 0.01%. Overall, the BOA SBAF model provides calibration coefficients with higher accuracy. The results suggest that the impact of spectral interpolation methods, BRDF model construction methods, and geometric matching on the proposed calibration model was relatively small.

In the future, the BOA SBAF model will be employed to cross calibrate the COCTS sensor over a longer time series.

In addition, the radiation degradation of the COCTS sensor throughout its operational period will be discussed.

ACKNOWLEDGMENT

The HY-1C satellite data were obtained from the website: https://osdds.nsoas.org.cn, Sentinel-2 and Sentinel-3 satellite data were obtained from the website: https://scihub.copernicus.eu, and MODIS satellite data were obtained from the website: https://ladsweb.modaps.eosdis.nasa.gov. The authors would like to thank the National Satellite Ocean Application Service, the European Space Agency, and the National Aeronautics and Space Administration for providing data support. The authors would also like to thank the anonymous reviewers.

REFERENCES

[1] C. Hu, Z. Lee, and B. Franz, "Chlorophyll *a* algorithms for oligotrophic oceans: A novel approach based on three-band reflectance difference," *J. Geophys. Res.: Oceans*, vol. 117, Jan. 2012, Art. no. C01011.

[2] M. J. Behrenfeld et al., "Climate-driven trends in contemporary ocean productivity," *Nature*, vol. 444, no. 7120, pp. 752–755, 2006.

[3] A. Kuze et al., "Long-term vicarious calibration of GOSAT short-wave sensors: Techniques for error reduction and new estimates of radiometric degradation factors," *IEEE Trans. Geosci. Remote Sens.*, vol. 52, no. 7, pp. 3991–4004, Jul. 2014.

[4] K. Tan et al., "Vicarious calibration for the AHSI instrument of Gaofen-5 with reference to the CRCS Dunhuang test site," *IEEE Trans. Geosci. Remote Sens.*, vol. 59, no. 4, pp. 3409–3419, Apr. 2021.

[5] L. Liu, T. Shi, H. Gao, X. Zhang, Q. Han, and X. Hu, "Long-term cross calibration of HJ-1A CCD1 and Terra MODIS reflective solar bands," *Sci. Rep.*, vol. 11, no. 1, Apr. 2021, Art. no. 7386.

[6] J. Han, Z. Tao, Y. Xie, Q. Liu, and Y. Huang, "Radiometric cross-calibration of GF-4/PMS based on radiometric block adjustment," *IEEE Trans. Geosci. Remote Sens.*, vol. 59, no. 6, pp. 4522–4534, Jun. 2021.

[7] M. M. Farhad, M. Kaewmanee, L. Leigh, and D. Helder, "Radiometric cross calibration and validation using 4 angle BRDF model between Landsat 8 and Sentinel 2A," *Remote Sens.*, vol. 12, no. 5, Mar. 2020, Art. no. 806.

[8] J. Han and Y. Xie, "Image dodging algorithm for GF-1 satellite WFV imagery," *Acta Geodaetica Cartographica Sinica*, vol. 45, no. 12, pp. 1423–1433, Dec. 2016.

[9] L. Juan, F. Lian, and P. Xiaoping, "Comparison of the cross-calibration methods between image-based and RTM-BRDF for GF-1 images," *Acta Geodaetica Cartographica Sinica*, vol. 46, no. 7, pp. 882–890, Jul. 2017.

[10] L. Feng, J. Li, W. Gong, X. Zhao, X. Chen, and X. Pang, "Radiometric cross-calibration of Gaofen-1 WFV cameras using Landsat-8 OLI images: A solution for large view angle associated problems," *Remote Sens. Environ.*, vol. 174, pp. 56–68, Mar. 2016.

[11] Q. Zhou, L. Tian, J. Li, and W. Li, "Assessment of bidirectional reflectance effects on desert and forest for radiometric cross-calibration of satellite sensors," *ISPRS J. Photogrammetry Remote Sens.*, vol. 160, pp. 180–194, Feb. 2020.

[12] J. Han et al., "Radiometric cross-calibration of GF-6/WFV sensor using MODIS images with different BRDF models," *IEEE Trans. Geosci. Remote Sens.*, vol. 60, 2022, Art. no. 5409311.

[13] J. Czapla-Myers, K. Thome, B. Wenny, and N. Anderson, "Railroad valley radiometric calibration test site (RadCaTS) as part of a global radiometric calibration network (RadCalNet)," in *Proc. IEEE Int. Geosci. Remote Sens. Symp.*, 2020, pp. 6413–6416.

[14] G. H. Tilstone et al., "Performance of ocean colour Chlorophyll a algorithms for Sentinel-3 OLCI, MODIS-Aqua and Suomi-VIIRS in open-ocean waters of the Atlantic," *Remote Sens. Environ.*, vol. 260, Jul. 2021, Art. no. 112444.

[15] Y. Xie, J. Han, X. Gu, and Q. Liu, "On-orbit radiometric calibration for a space-borne multi-camera mosaic imaging sensor," *Remote Sens.*, vol. 9, no. 12, Dec. 2017, Art. no. 1248.

[16] L. Yan, J. Li, and C. Xiao, "Vicarious radiometric calibration of the AHSI instrument onboard ZY1E on Dunhuang radiometric calibration site," *IEEE Trans. Geosci. Remote Sens.*, vol. 60, 2022, Art. no. 5530713.

[17] X. Hu et al., "Characterization of CRCS Dunhuang test site and vicarious calibration utilization for Fengyun (FY) series sensors," *Can. J. Remote Sens.*, vol. 36, no. 5, pp. 566–582, Oct. 2010.

[18] L. Liu et al., "Satellite-based time series calibration of GF-1 WFV sensors for large view zenith angle observations," *Int. J. Remote Sens.*, vol. 39, no. 22, pp. 8293–8316, 2018.

[19] L. Xiaoying et al., "Radiometric cross-calibration of the CBERS-02 CCD camera with the TERRA MODIS," *Sci. China Technol. Sci.*, vol. 48, no. S2, pp. 44–60, Mar. 2005.

[20] B. Zhong, Y. Zhang, T. Du, A. Yang, W. Lv, and Q. Liu, "Cross-calibration of HJ-1/CCD over a desert site using Landsat ETM + imagery and ASTER GDEM product," *IEEE Trans. Geosci. Remote Sens.*, vol. 52, no. 11, pp. 7247–7263, Nov. 2014.

[21] J. Lu, T. He, S. Liang, and Y. Zhang, "An automatic radiometric cross-calibration method for wide-angle medium-resolution multispectral satellite sensor using landsat data," *IEEE Trans. Geosci. Remote Sens.*, vol. 60, 2022, Art. no. 5604011.

[22] X. Zhou, D. Feng, Y. Xie, Z. Tao, T. Lv, and J. Wang, "Radiometric cross-calibration of GF-4/IRS based on MODIS measurements," *IEEE J. Sel. Topics Appl. Earth Observ. Remote Sens.*, vol. 14, pp. 6807–6814, 2021.

[23] E. Reitshamer, K. Barrett, K. Shea, and B. Dawson-Hughes, "Cross-calibration of prodigy and horizon a densitometers and precision of the horizon a densitometer," *J. Clin. Densitometry*, vol. 24, no. 3, pp. 474–480, Feb. 2021.

[24] J. Han, Z. Tao, Y. Xie, H. Li, Q. Liu, and X. Guan, "A novel radiometric cross-calibration of GF-6/WFV with MODIS at the Dunhuang radiometric calibration site," *IEEE J. Sel. Topics Appl. Earth Observ. Remote Sens.*, vol. 14, pp. 1645–1653, 2021.

Yong Xie (Senior Member, IEEE) received the B.S. and M.S. degrees in physics from Nanjing Normal University, Nanjing, China, in 2000 and 2004, respectively, and the Ph.D. degree in earth science and geoinformation system from George Mason University, Fairfax, VA, USA, in 2009.

He is currently a Professor with the School of Geographical Science, Nanjing University of Information Science and Technology, Nanjing. He has worked on the radiomimetic calibration and characterization of satellite remote sensor and science product validation with ground measurements.

Duo Feng received the B.S. degree in geographic information science in 2021 from the Nanjing University of Information Science and Technology, Nanjing, China, where he is currently working toward the M.S. degree in geography.

His research interests include satellite sensor on-orbit radiometric calibration.

Wen Shao received the B.E. in communications engineering and M.Eng. degrees in electronics and communication engineering, from the Nanjing University of Information Science and Technology Nanjing, China, in 2017 and 2020, where he is currently working toward the Ph.D. degree in 3S integration and meteorological applications.

His research interests include satellite sensor on-orbit radiometric calibration.

Jie Han received the B.S. and M.S. degrees in science and technology of surveying and mapping from Henan Polytechnic University, Jiaozuo, China, in 2009 and 2012, respectively, and the Ph.D. degree in geography and geographic information system from the Institute of Remote Sensing and Digital Earth, Chinese Academy of Sciences, Beijing, China, in 2015.

He is currently an Associate Professor with the School of Geography and Geomatics, Xuchang University, Xuchang, China. He has worked on the radiomimetic and geometric processing of remote sensing images. His main research interests include quantitative remote sensing applications in the visible/near-infrared region.

Yidan Chen received the B.E. degree in surveying engineering from Xuchang University, Xuchang, China, in 2022. She is currently working toward the master's degree in 3S integration and meteorological applications with the Nanjing University of Information Science and Technology, Nanjing, China.

Her main research interests include satellite sensor on-orbit radiometric calibration.